Article

A DFT Study of CO Hydrogenation on Graphene Oxide: Effects of Adding Mn on Fischer–Tropsch Synthesis

Hanieh Bakhtiari [1], Saeedeh Sarabadani Tafreshi [1,2,*], Mostafa Torkashvand [1], Majid Abdouss [1] and Nora H. de Leeuw [2,3,*]

1 Department of Chemistry, Amirkabir University of Technology, No. 350, Hafez Avenue, Valiasr Square, Tehran 1591634311, Iran; bakhtiaryhani1998@gmail.com (H.B.); mostafa.t@aut.ac.ir (M.T.); phdabdouss44@aut.ac.ir (M.A.)

2 School of Chemistry, University of Leeds, Leeds LS2 9JT, UK

3 Department of Earth Sciences, Utrecht University, 3584 CB Utrecht, The Netherlands

* Correspondence: s.s.tafreshi@aut.ac.ir or s.sarabadanitafreshi@leeds.ac.uk (S.S.T.); n.h.deleeuw@leeds.ac.uk or n.h.deleeuw@uu.nl (N.H.d.L.)

Abstract: The hydrogenation of carbon monoxide (CO) offers a promising avenue for reducing air pollution and promoting a cleaner environment. Moreover, by using suitable catalysts, CO can be transformed into valuable hydrocarbons. In this study, we elucidate the mechanistic aspects of the catalytic conversion of CO to hydrocarbons on the surface of manganese-doped graphene oxide (Mn-doped GO), where the GO surface includes one OH group next to one Mn adatom. To gain insight into this process, we have employed calculations based on the density functional theory (DFT) to explore both the thermodynamic properties and reaction energy barriers. The Mn adatoms were found to significantly activate the catalyst surface by providing stronger adsorption geometries. Our study concentrated on two mechanisms for CO hydrogenation, resulting in either CH_4 production via the reaction sequence $CO \rightarrow HCO \rightarrow CH_2O \rightarrow CH_2OH \rightarrow CH_2 \rightarrow CH_3 \rightarrow CH_4$ or CH_3OH formation through the $CO \rightarrow HCO \rightarrow CH_2O \rightarrow CH_2OH \rightarrow CH_3OH$ pathway. The results reveal that both products are likely to be formed on the Mn-doped GO surface on both thermodynamic grounds and considering the reaction energy barriers. Furthermore, the activation energies associated with each stage of the synthesis show that the conversion reactions of $CH_2 + OH \rightarrow CH_3 + O$ and $CH_2O + OH \rightarrow CH_2OH + O$ with energy barriers of 0.36 and 3.86 eV are the fastest and slowest reactions, respectively. The results also indicate that the reactions: $CH_2OH + OH \rightarrow CH_2 + O + H_2O$ and $CH_2OH + OH \rightarrow CH_3OH + O$ are the most exothermic and endothermic reactions with reaction energies of −0.18 and 1.21 eV, respectively, in the catalytic pathways.

Keywords: carbon monoxide hydrogenation; CH_4; catalyst; Mn-doped graphene oxide; DFT

1. Introduction

Urban environments represent intricate networks of ever-expanding infrastructure that pose potential health risks to a significant portion of their inhabitants [1–5]. Air pollution is a leading contributor to health problems in modern urban life [6]. In urban environments, air pollutants originate from various natural and anthropogenic sources, primarily owing to the incomplete combustion of fossil fuels, particularly in transportation [7]. Carbon monoxide (CO) is a notable yet often imperceptible air pollutant [8,9].

Fischer–Tropsch synthesis (FTS) and the oxidation of CO are two different approaches for the conversion of CO into useful or more benign products. Fischer–Tropsch synthesis is a widely used but complex process that converts syngas (a mixture of CO and hydrogen) into a wide spectrum of hydrocarbons and oxygenates [10–21]. This process involves the hydrogenation of adsorbed CO, leading to the formation of CH_xO species and subsequent C–O bond cleavage, followed by the removal of adsorbed oxygen species [22–27]. The FTS process offers several advantages, including adaptability to diverse feedstocks for the

production of liquid fuels and chemicals. It is particularly valuable in several industries, and is capable of generating high-quality diesel and jet fuels that meet strict environmental standards. FTS can also utilize renewable sources like biomass, contributing to a more sustainable and circular economy. However, this process has drawbacks, notably the significant energy required for syngas production, which results in high operational costs and negative environmental impacts. Moreover, FTS demands substantial financial investment, making it economically feasible only for large-scale operations and creating barriers for smaller enterprises [28–30].

In contrast, the oxidation of carbon monoxide (CO) offers a straightforward and efficient method for converting CO into non-toxic carbon dioxide (CO_2) [28–30]. Despite its safety and simplicity, this reaction has limitations, including the lack of useful byproducts and the need for expensive catalysts. Additionally, CO oxidation produces a major greenhouse gas, and our research is therefore focused on CO hydrogenation within the FTS framework, aiming to convert CO into more valuable substances [28–30].

The FTS process proceeds at the active sites on metal catalyst surfaces. Several alternative catalysts have been examined for their potential to catalyze CO hydrogenation [31–34]. Mn-modified graphene has been predicted to be a promising catalyst for CO oxidation, whereas in an investigation of the binding abilities of transition metals (TMs) to graphene nanoflakes (GNFs), Mn-GNF was found to have a relatively high adsorption energy for CO. Another study found that Mn-embedded di-vacancy graphene is an efficient catalyst for CO oxidation at low temperature [35,36].

Graphene oxide (GO) is a unique material that can be viewed as a single monolayer [37]. It is a heterogeneous, inexpensive, and environmentally friendly carbo-catalyst [38]. Under specific oxidizing conditions, carbon atoms maintain the integrity of the 2D layered structure with oxygen-containing functional groups attached to both sides of the carbon plane and edges [39]. Graphene oxide demonstrates significantly higher chemical activity than graphene [40–42]. Lahaye et al. conducted DFT studies to illuminate the structure of GO, shedding light on the arrangement of hydroxyls and oxygens on GO layers. Their findings revealed a moderate wrinkling of the carbon skeleton in GO with 1,2 ethers, predominantly due to locally induced sp3 hybridization, while maintaining a hexagonal structure akin to graphene [43].

The literature has shown that metal-doped graphene and graphene oxide surfaces also have high catalytic activity toward CO hydrogenation. In the field of carbon monoxide (CO) methanation, nickel (Ni) and iron (Fe) catalysts have commonly been applied due to their catalytic efficiency in enabling the hydrogenation process. The emergence of graphene oxide (GO) as a catalyst or catalyst-support material thus signifies a significant shift, which is attributed to its outstanding physicochemical characteristics. The expansive surface area of GO enhances the dispersion of metal adatoms, thereby improving the catalytic interface [44]. Its strong thermal and chemical durability is beneficial for reactions that require high-temperature conditions [44]. When employed as a supporting framework, GO has the potential to affect catalytic activity, selectivity, and durability, possibly leading to synergistic effects when combined with transition metals such as Ni or Fe [45]. Although Ni-based catalysts are attractive as they are cost-effective and abundant, they are, however, vulnerable to sintering and subsequent reduction in activity at elevated temperatures [46]. In contrast, Fe-based catalysts, particularly bimetallic compositions with Ni, can overcome these challenges, providing improved catalytic stability and efficiency [47]. Gui et al. [48] used density functional theory (DFT) calculations to study the adsorption and gas-sensing properties of CH_4, C_2H_2, and CO on Mn-graphene. They found that among the three typical doping sites of Mn on graphene, Mn doping in a bridge site was more stable than in the other two sites (top and hollow sites), which was then chosen for further gas adsorption studies. Their results revealed that CH_4 adsorbs close to the Mn atom through its H atom, whereas C_2H_2 and CO adsorption occurs directly above Mn through their C atoms. They also found that Mn-graphene is insensitive to CH_4 gas, but could be an optimal gas-sensing material for C_2H_2 and CO detection. Wei et al. [49] studied the CO

hydrogenation performance of iron oxide/rGO catalysts and provided an efficient strategy for the rational design of carbon-supported iron-based CO hydrogenation catalysts. Their results showed that the use of GO is a favorable and efficient method for enhancing the CO hydrogenation performance of iron-based catalysts, where the reactants were reported to be inexpensive and of low toxicity. The added organics selectively adsorbed on the iron precursor or GO can modify the metal–support interaction, which further affects the physicochemical properties and, thus, the CO hydrogenation performance. Mn can enhance the adsorption capacity of CO by increasing the surface charge density of Fe, which makes it easier for CO molecules to bind to the catalyst surface. This could improve the activity towards FTS because more CO molecules can react with hydrogen to form hydrocarbons. Mn can also promote the formation of iron carbide by facilitating the dissociation of CO and diffusion of carbon atoms into the iron lattice. Iron carbide is the main active phase for FTS, as it can catalyze the chain propagation reaction, which is the key step in the production of long-chain hydrocarbons [50]. Mn is better than other transition metals for three reasons: (i) Mn can enhance the adsorption capacity of CO and promote the formation of iron carbide, which are the active species for FTS [50,51], (ii) Mn can suppress CH_4 formation and facilitate the carbon chain growth, which can increase the selectivity of C5+ long-chain hydrocarbons and the olefin to paraffin ratio [50–52], and (iii) Mn can increase the CO conversion and the selectivity of light olefins, which are valuable petrochemical feedstocks [53]. Zafari et al. [54] reported light olefin selectivity over Co–Mn bimetallic catalysts supported on graphene and reduced graphene oxide. These studies have contributed to our understanding of catalyst behavior in CO hydrogenation.

Based on these insights, GO-based catalysts have demonstrated potential for gas adsorption and catalyzed reactions, and Mn doping can improve the catalytic performance. Therefore, in this DFT study, Mn-doped GO was chosen as the catalyst for CO hydrogenation through FTS.

2. Results and Discussion

2.1. GO Surface

The hexagonal graphene cell was constructed by a $5 \times 5 \times 1$ extension of the primitive cell of graphene containing 50 carbon atoms with dimensions of 12.339×12.339 Å, Figure 1A. A vacuum of almost 25 Å was added on top of the slab to avoid interactions between slab images in the Z direction of the cell. We have utilized a 5×5 graphene supercell in our density functional theory (DFT) calculations. This selection was guided by a delicate equilibrium between the need for a substantial model that could effectively mitigate issues related to edge effects and interactions occurring amidst periodic images, and the potentially prohibitive computational cost. A supercell with these dimensions is sufficient to elucidate the fundamental characteristics of the catalytic surface and investigate the adsorption phenomena and catalytic reactions without undue distortions induced by artificial confinements typically encountered in smaller simulation cells. In addition, the 5×5 supercell has been reported before in the literature, thus ensuring that our findings can be compared directly with previous works. The selection of a specific quantity of graphene primitive cells contained within this larger cell was made with careful consideration of the need to create sufficient potential adsorption sites to study the different catalytic processes.

One OH group was added onto the graphene surface to model a GO surface, and we systematically explored various positions on the GO surface to determine the most suitable location for the Mn atom. Multiple optimization calculations were conducted to attain a stable GO surface in the presence of Mn. We have considered various positions for the manganese on the catalyst surface, i.e., atop, bridging, or within honeycomb sites. We found that the Mn located at the honeycomb site was the only stable position for the Mn atom, with the OH adsorbed on top of the carbon surface atom next to the Mn atom via its O atom, as depicted in Figure 1B.
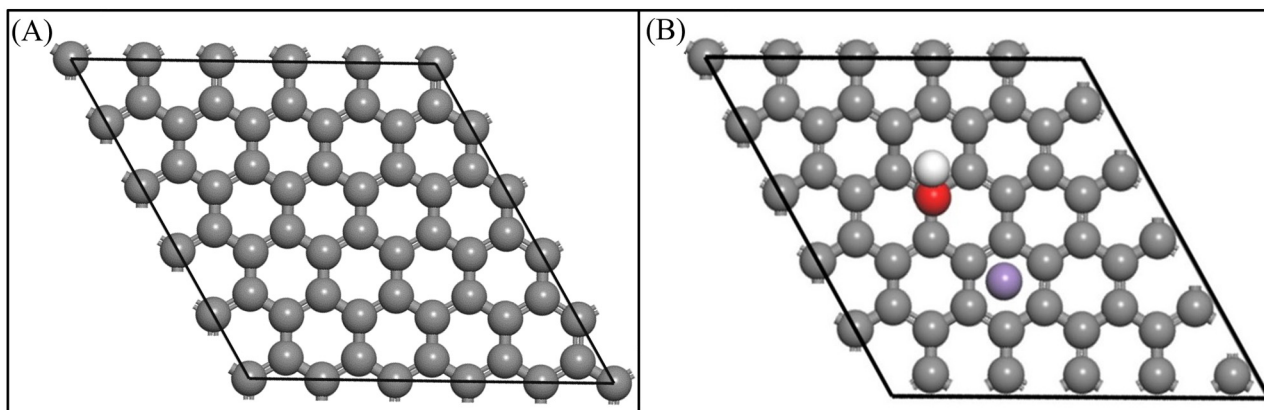
Figure 1. Top views of the hexagonal cell of (**A**) graphene, and (**B**) Mn-doped GO monolayers. Carbon, oxygen, hydrogen, and manganese atoms are shown in gray, red, white, and purple, respectively.

In Figure 2, we observe distinct charge transfer when a hydroxide species is adsorbed on the graphene surface, indicating significant intermolecular interaction. Such interactions are precursors for chemical bond formation, leading to a substantial reconfiguration of the electronic structure of the surface, that could affect the surface reactivity.
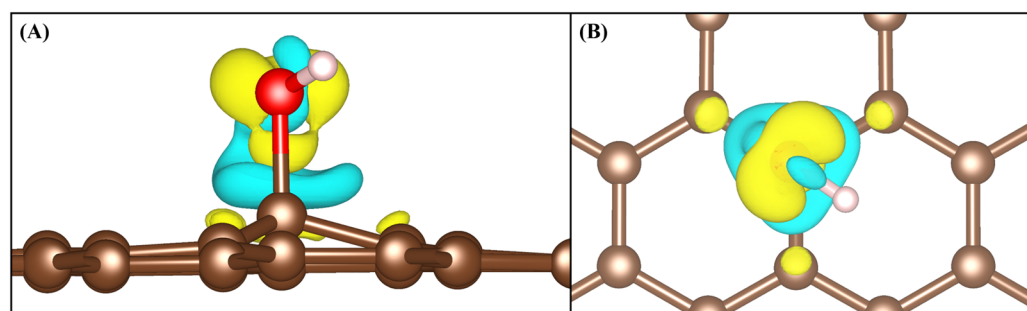

Figure 2. (**A**) side, and (**B**) top views of charge density differences caused by the adsorption of OH on GO. The blue and yellow iso-surfaces indicate charge depletion and accumulation, with the iso-surface value set to ± 0.01. Carbon, oxygen, and hydrogen atoms are shown in gray, red, and white, respectively.

2.2. Thermodynamic Analysis

2.2.1. Adsorption Energies

We investigated the formation of CH_4 and CH_3OH, both of which are the products of the FTS reaction (Table 1). We first calculated the adsorption energy (E_{ads}) and the nearest distances between the surface atoms and the atoms of the adsorbate molecules.

Table 1. Reaction pathways for the synthesis of methane (CH_4) and methanol (CH_3OH) on Mn-doped GO surface.

Methane Pathway	Methanol Pathway
$CO + OH \rightarrow HCO + O$	$CO + OH \rightarrow HCO + O$
$HCO + OH \rightarrow CH_2O + O$	$HCO + OH \rightarrow CH_2O + O$
$CH_2O + OH \rightarrow CH_2OH + O$	$CH_2O + OH \rightarrow CH_2OH + O$
$CH_2OH + OH \rightarrow CH_2 + O + H_2O$	$CH_2OH + OH \rightarrow CH_3OH + O$
$CH_2 + OH \rightarrow CH_3 + O$	-
$CH_3 + OH \rightarrow CH_4 + O$	-

In the Fischer–Tropsch reaction, both CH_4 and CH_3OH products undergo similar reactions but lead to distinct outcomes, and CO, acting as the reactant, gives rise to both products. Hence, the molecules were positioned in close proximity to the metal catalyst (Mn) on the surface. This strategic placement is essential for facilitating the relevant reactions that lead to the formation of CH_4 and CH_3OH. In this study, we propose a reaction pathway where hydrogen from the hydroxyl group of the GO transfers to the intermediates and the remaining oxygen from the hydroxyl group adsorbs on the carbon surface atoms as an epoxy group, as seen in other experimental and theoretical studies [55–57]. We employ a model proposed for the conversion of carbon monoxide to methane and methanol on a Mn-doped GO surface to simulate the likely route of carbon monoxide reduction, as shown in Table 1, where we have focused on the fundamental CO + OH → HCO + O reaction [55]. For both methane and methanol formation, we suggest a comparable scheme where the initial, second, and third stages of hydrogenation are identical to minimize the number of reactions to reach the products (Table 1). Our proposed mechanism does not include the CO hydrogenation to COH reaction, due to the instability of COH on Mn-doped GO. Moreover, we have not considered the CO dissociation reaction, as we aimed to minimize the pathway by solely focusing on the hydrogenation of CO without disrupting its bond, in alignment with previous studies on GO catalysts [54,55].

We calculated the adsorption energies of the intermediate structures on the Mn-doped GO surface in the presence of a hydroxide that provides hydrogen to initiate the carbon monoxide hydrogenation. We calculated the formation energies of both graphene surfaces with hydroxide and manganese catalysts as well as graphene surfaces with only manganese metal. The formation energies for the graphene surface with hydroxide and manganese catalysts and for the graphene surfaces with only manganese metal catalysts are −3.125 eV and −1.378 eV, respectively, indicating that the presence of hydroxides stabilizes the Mn-doped graphene surface.

For each molecule on the catalytic surface, we sought to determine the most stable geometric structure and the best mode of adsorption by placing the molecules at various sites and in different configurations on the surface. Figure 3 shows the various interactions between the adsorbed molecules and the Mn-doped GO surface. Because the CO molecule does not adsorb on the pure GO surface, no reaction can take place on the catalytic surfaces of GO in the absence of Mn, in agreement with previous experimental and computational studies [1].

In Table 2, we report the adsorption energies related to the molecular species in the initial steps of the Fischer–Tropsch reaction for both methane and methanol.

Table 2. Adsorption energies and bond lengths of intermediates on the Mn-doped GO surface. The results of other studies were added for comparison [48,58–62].

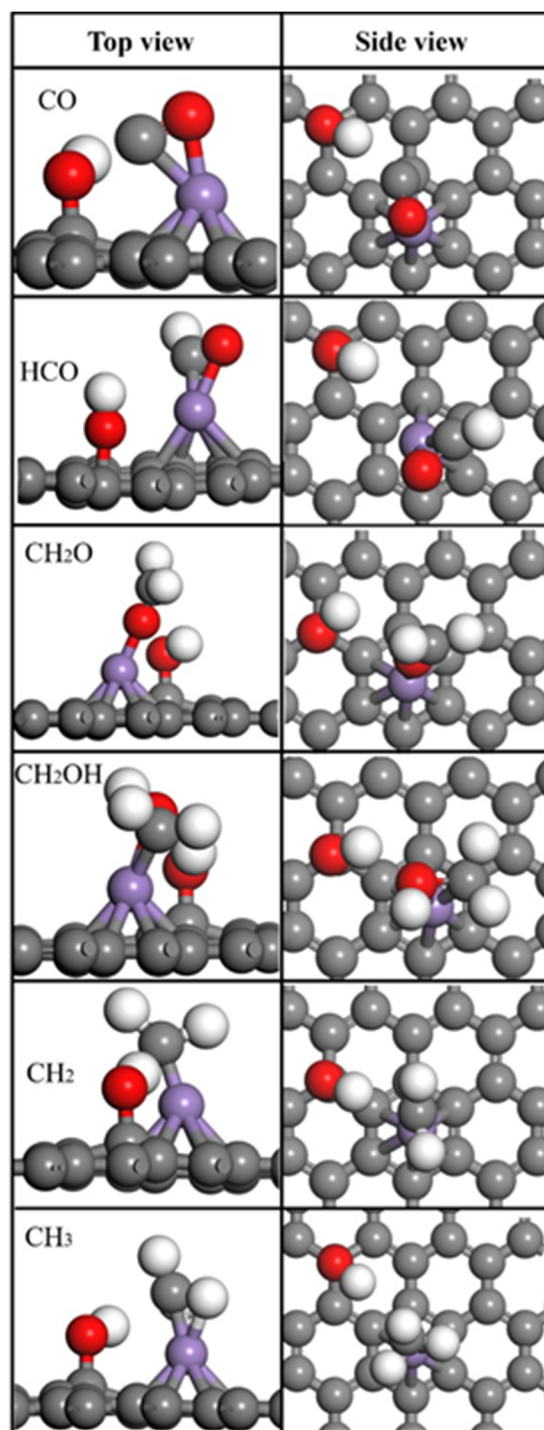| Bond Length (Gr and Mol) (Å)		Bond Length (Mn and Mol) (Å)	E_{ads} (eV)	E_{ads} (eV) (Other Studies)
(Gr−O) 3.78 (Gr−C) 2.88	CO	(Mn−O) 1.92 (Mn−C) 1.97	−1.35	−1.95 [48] Mn-doped graphene −1.16 [58] Phosphorene
(Gr−O) 3.62 (Gr−C) 3.24	HCO	(Mn−O) 1.99 (Mn−C) 1.79	−3.27	−2.96 [59] Cu–Co (111) and (211) −3.63 [60] fccMo₂C (100)
(Gr−O) 3.26	CH₂O	(Mn−O) 1.78	−2.04	−2.52 [60] fccMo₂C (100) −2.23 [61] ZnO nano-cage
(Gr−O) 3.38 (Gr−C) 3.17	CH₂OH	(Mn−O) 2.07 (Mn−C) 1.94	−3.61	−3.09 [60] fcc-Mo₂C (100)
(Gr−C) 3.30	CH₂	(Mn−C) 1.70	−5.58	−5.54 [62] Cu-based alloys
(Gr−C) 3.42	CH₃	(Mn−C) 1.79	−3.48	−3.26 [59] Cu-Co (111) and (211) −3.55 [60] fcc-Mo₂C (100)

Figure 3. Adsorption geometries of the studied molecules during CO hydrogenation on Mn-doped GO surface. The gray, white, red, and purple balls represent carbon, hydrogen, oxygen, and manganese atoms, respectively.

The reactions were performed on the primary surface of the Mn-doped GO adatom catalyst. The molecules of interest were positioned on the surface slab to observe their interactions with the hydroxide groups in proximity to the catalyst. Through a series of optimizations of the molecules at different locations across the slab, it was established that the most favorable position for the molecules was the manganese metal catalyst.

Through a comparison of the adsorption energies, molecular separations from the graphene surface, and interactions with the Mn catalyst, we evaluated the impact of the

hydroxide group on the GO surface. The Mn catalyst significantly activated the surface, resulting in larger adsorption energies and further separation between molecules and the graphene surface. Moreover, the larger adsorption energies and longer distances show that the addition of hydroxide groups to the GO surfaces considerably improved the processes. Our results highlight the critical functions of the hydroxide group and manganese catalyst in promoting molecular adsorption and reactions on the GO surface. However, further investigation into the underlying mechanisms is necessary to improve the reaction conditions for use in practical systems.

Among the molecules studied, CH_2 releases the largest adsorption energy (-5.80 eV), indicating its stability on the catalyst surface and likely participation in hydrocarbon production. Its adsorption energy compares well with the reference value of -5.54 eV [62] observed on Cu-based alloys.

In terms of stability for CH_3OH synthesis, HCO, with an adsorption energy of -3.27 eV, is between CH_2 and CH_2OH, possibly functioning as an essential intermediary. CH_3 might provide a less significant contribution to the process because of its relatively smaller adsorption energy (-3.48 eV). CH_2OH, while having a smaller adsorption energy (-3.61 eV) compared to CH_2 and CH_2OH in CH_3OH formation, is still relatively stable at the surface, suggesting its potential involvement in hydrocarbon generation. CH_2O, with the smallest adsorption energy (-2.04 eV) among the considered molecules, may therefore only participate to a limited degree in the reaction. CO, having the smallest adsorption energy (-1.35 eV) among all molecules, is the least stable and plays a less significant role in the reaction on this catalyst surface. These results collectively offer valuable insights into the stability and reactivity of various molecules on the Mn-doped GO surface, which could prove instrumental in catalyst design and optimization for FTS.

The adsorption of CO in the $CO + OH \rightarrow HCO + O$ reaction is a pivotal step in FTS and greatly influences its outcomes. DFT calculations have been employed to scrutinize the adsorption energy of CO on diverse catalytic surfaces. Notably, the computed adsorption energy of CO on Mn-doped GO is -1.35 eV, indicating its potential as a reactant in various syntheses. Other materials such as Mn-doped graphene (-1.95 eV) [48] and phosphorene (-1.16 eV) [58] exhibit similar adsorption energies for CO as to Mn-doped GO, signifying their potential as catalysts for CO adsorption in FTS. It is crucial to recognize that the choice of catalyst significantly affects the chemical reaction rate and product selection in FTS. Therefore, in-depth research is imperative to unravel the underlying mechanisms governing CO adsorption on different catalysts, facilitating the development of efficient catalysts suitable for industrial-scale FTS.

In the $CH_2O + OH \rightarrow CH_2OH + O$ reaction, CH_2O generates the largest adsorption energy (-2.04 eV) among the molecules under consideration on the Mn-doped GO surface, binding a little more strongly to the Mn-doped GO than, for example, to the fcc-Mo_2C (100) surface at -1.86 eV [60], but less so than on the ZnO nano-cage surface at -2.23 eV [61]. This indicates its relative stability at the surface and suggests that it might be less likely to take part in reactions compared to molecules like CH_2 or CH_2OH.

The subsequent phase of our research focused on analyzing the products of reactions involving epoxy as a by-product. In our investigation, we discerned distinct variations in the characteristics of GO and epoxy, Mn, and the initial surface adsorption energy with OH during the synthesis. These discrepancies serve as crucial indicators, delineating the transformation from the initial stages to the final products in each reaction, providing valuable insights into the synthesis dynamics. The favorable adsorption of molecules on the surface decreased, facilitating their mobility, and enabling the formation of the desired product. Another crucial observation was the change in the distance between the molecules and the Mn atom during this process. After hydrogenation, all of the reaction products exhibited a surface with epoxy, and we identified differences between this modified slab and the original one. These results underscored the activation of the slab and its transformation into an improved surface for catalytic reactions. Similar to the hydroxyl groups, the epoxy groups on Mn-doped graphene oxide surfaces play a crucial

role in regulating the adsorption and reaction energy in CO hydrogenation. These groups alter the electronic structure of the catalyst, thereby affecting the adsorption of reactants. In agreement with other studies, epoxy groups acting as active sites can lower activation energies, stabilize chemical intermediates, and improve charge transfer, thereby impacting the reaction energy barriers and thermodynamics of the reaction. Their presence promotes catalytic efficiency, ultimately affecting the selectivity towards methane and methanol production [63–66].

2.2.2. Reaction Energies

Table 3 presents the calculated reaction energies of the investigated reactions. Due to the low reaction energy (0.05 eV), the interaction of CO with OH to produce HCO and O is relatively easy to achieve. The conversion of CO to HCO, a precursor to longer-chain hydrocarbons, is initiated through this reaction, whereas the reaction between HCO and OH, resulting in CH_2O and O with a reaction energy of 0.41 eV, is more endothermic.

Table 3. The calculated reaction energies on the Mn-doped GO surface.

Reactions	Thermal Properties	$E_{reaction}$ (eV)
$CO + OH \rightarrow HCO + O$	ENDO	0.05
$HCO + OH \rightarrow CH_2O + O$	ENDO	0.41
$CH_2O + OH \rightarrow CH_2OH + O$	ENDO	0.29
$CH_2OH + OH \rightarrow CH_2 + O + H_2O$	EXO	−0.18
$CH_2 + OH \rightarrow CH_3 + O$	ENDO	0.33
$CH_3 + OH \rightarrow CH_4 + O$	ENDO	0.71
$CH_2OH + OH \rightarrow CH_3OH + O$	ENDO	1.21

The reaction of CH_2O with OH, forming CH_2OH and O, has an intermediate reaction energy of 0.29 eV, indicating somewhat lower favorability than the CO + OH reaction. The reaction of CH_2OH with OH to form CH_2, O, and H_2O is exothermic with a reaction energy of −0.18 eV, and this is a crucial step as it leads to the formation of H_2O and other hydrocarbons. CH_2 reacting with OH to form CH_3 and O has a reaction energy of 0.33 eV, suggesting reduced favorability. However, it is not highly endothermic and could therefore contribute to longer-chain hydrocarbon formation. The reaction of CH_3 with OH to form CH_4 and O has the highest reaction energy among those discussed, at 0.71 eV, making it the least favorable. Nonetheless, it is a crucial reaction as it leads to methane formation.

Finally, the reaction of CH_2OH with OH to form CH_3OH and O has a relatively high endothermic reaction energy of 1.21 eV, although this reaction is significant for methanol formation. Thus, the most favorable reaction is CH_2OH with OH, forming CH_2, O, and H_2O, while the least favorable is CH_2OH with OH, forming CH_3OH and O. The energies of the other reactions vary between these extreme values but are largely achievable.

2.3. Reaction Energy Barrier Analysis

2.3.1. Activation Energies

During a chemical reaction, the participating molecules absorb thermal energy from their surroundings. This added energy boosts their movement, increasing the frequency and intensity of collisions while also encouraging atomic and bond vibrations within the molecules. This thermal agitation makes it more likely for chemical bonds to break. When a reactant molecule absorbs sufficient energy to reach the transition state, the reaction can proceed. Comparing activation energies for various key atmospheric reactions offers insight into the relative significance of each reaction under different conditions (see Table 4). The initial, transition and final states of the studied reactions are presented in Figure 4. In the first step, reaction $CO + OH \rightarrow HCO + O$ has a notably high activation energy of 2.48 eV which suggests a requirement for higher temperatures, whereas the following reaction,

HCO + OH → CH$_2$O + O, featuring a low activation energy of 0.48 eV, indicates greater efficiency at lower temperatures.

Table 4. Calculated activation energies ($E_{activation}$) for all reactions on the Mn-doped GO surface. The results of other studies were added for comparison [61,67–71].

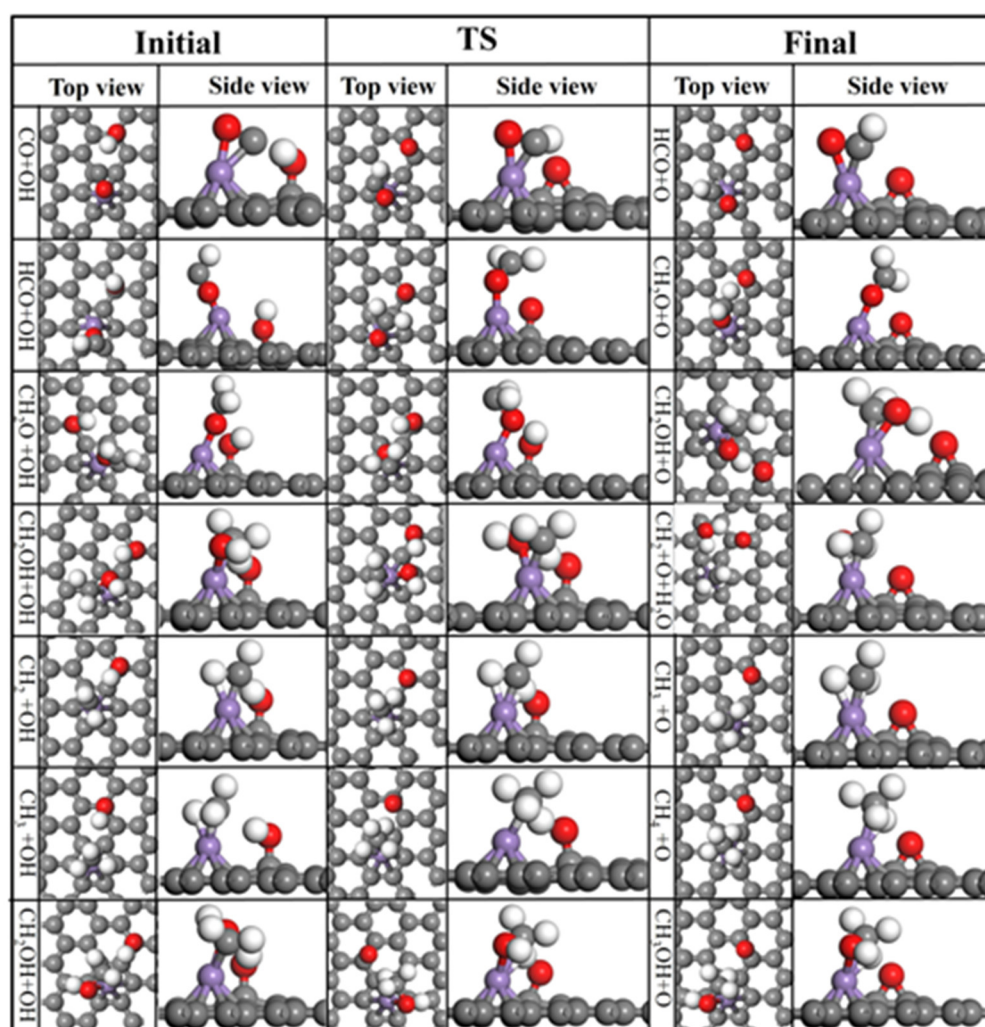| Reactions	$E_{activation}$ (eV)	$E_{ativation}$ (eV) (Other Studies)
CO + OH → HCO + O	2.48	2.35 [67]
HCO + OH → CH$_2$O + O	0.48	0.41 [68], 0.67 [69]
CH$_2$O + OH → CH$_2$OH + O	3.86	3.73 [70]
CH$_2$OH + OH → CH$_2$ + O + H$_2$O	0.80	0.84 [71]
CH$_2$ + OH → CH$_3$ + O	0.36	0.42 [61]
CH$_3$ + OH → CH$_4$ + O	1.35	1.20 [61]
CH$_2$OH + OH → CH$_3$OH + O	1.66	1.43 [61]

Figure 4. The reactions with their corresponding initial, transition, and final states on the Mn-doped GO surface. The gray, white, red, and purple balls represent carbon, hydrogen, oxygen, and manganese atoms, respectively.

The reaction CH$_2$O + OH → CH$_2$OH + O needs to overcome an activation energy of 3.86 eV, making it feasible only at higher temperatures. On the other hand, the reaction CH$_2$OH + OH → CH$_2$ + O + H$_2$O benefits from a low activation energy of 0.80 eV, signifying higher efficiency at lower temperatures. The reaction CH$_2$ + OH → CH$_3$ + O has an activation energy of only 0.36 eV, but the activation energy of reaction CH$_3$ + OH → CH$_4$ + O

is higher again at 1.35 eV. Finally, reaction $CH_2OH + OH \rightarrow CH_3OH + O$ requires an activation energy of 1.66 eV to be overcome, making it again more likely to occur at higher temperatures.

Table 4 compares the activation energies of a number of chemicals catalyzed by different metals. The middle column shows the activation energy of the reaction catalyzed by manganese (Mn), a metal that efficiently converts carbon monoxide (CO) to methane (CH_4) and methanol (CH_3OH) in Fischer–Tropsch synthesis. The last column provides the activation energies for various metal-catalyzed reactions indicating that manganese has catalytic properties comparable to other metals in the traditional FTS [61].

In order to identify the rate equation of the reaction, the number of reaction steps, and the rate-determining step (RDS), we need to understand and control reaction rates. The RDS can be determined within a set of reactions by assessing their respective energy profiles. Within the context of our methane and methanol production reactions, $CH_2O + OH \rightarrow CH_2OH + O$ with its activation energy of 3.86 eV is the rate-determining step for these two reactions.

2.3.2. Reaction Profiles

The graph for methane production shows that the processes are mostly exothermic. The most exothermic steps are the reactions of $CH_2O + OH \rightarrow CH_2OH + O$ and $CO + OH \rightarrow HCO + O$, as shown in the diagram of methanol and methane formation (Figure 5). The energy difference between the initial and final states suggests that the formation of these two products leads to significant energy release. However, this stage of the reaction path is the slowest, as is clear from the activation energies in Table 4. After this step, the graph of the first path shows that the energies remain largely the same, illustrating that the reaction is moving quite rapidly in the direction of the product.
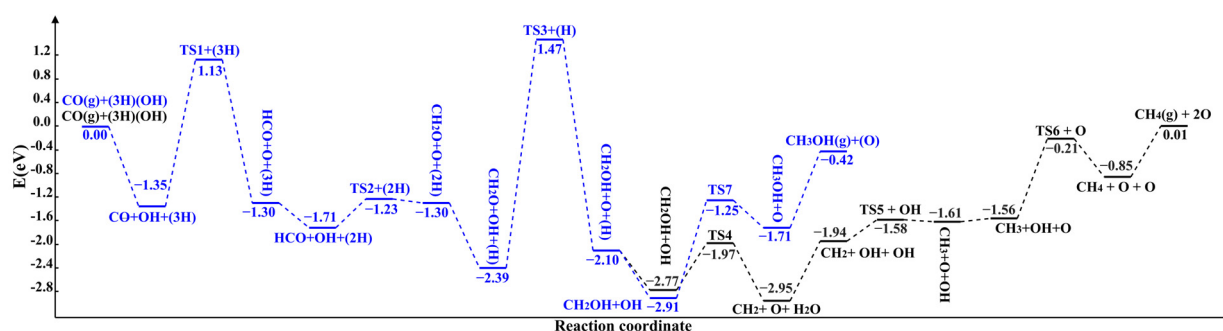

Figure 5. Reaction profile illustrating how the energies change in the pathway resulting in CH_4 and CH_3OH production.

As the reaction pathway unfolds, we observe gradual increments in the activation energy. When the levels of activation energy rise, the rate constant exhibits a corresponding decrease, providing insight into the point along the path where the rate is especially impacted. In this particular reaction, manganese works as a catalyst, effectively reducing the activation energies. Notably, the existence of this catalyst, as indicated in the absorption energy table (Table 2), results in a negative absorption energy on graphene oxide. This signifies that the molecules in each reaction release a significant amount of energy when they adsorb onto the surface, which facilitates the reactions. By closely examining the reaction pathways for both products, it is possible to conclude that the significant energy released corresponds to the activation energy required for each reaction and the heat absorption along this path. These results confirm the suitability of the catalyst and ultimately provide an explanation for the reaction's spontaneous progression, even allowing for the high activation energies. As such, reactions like $CH_2O + OH \rightarrow CH_2OH + O$, with an activation energy of 3.86 eV, are still likely to happen, as the absorption energy released within the reaction environment supplies enough energy to overcome the activation energy barrier and drive the reaction forward. Supporting evidence lies in the consistent

progress of the reaction, with slow-downs primarily manifesting during the intermediate stages and, to a lesser extent, in the final conversion from CH_2 to CH_4. The reaction does, however, appear to be slowing down in the pathway diagrams, particularly during the $CH_2O + OH \rightarrow CH_2OH + O$ generation stage, which has a peak energy of 3.86 eV but a net energy of -3.60 eV and is the rate-determining step. The final conversion of CH_2OH to methanol is an endothermic process, with the methane generation process continuing on.

Next, we performed a thermodynamic analysis of the transition states to locate the critical step, with a focus on finding steps that displayed exothermic behavior. After an exhaustive analysis of each step (as shown in Table 5), we found that the first three processes in the synthesis of both methanol and methane had the same thermodynamic exothermic properties. Step 3 (TS3 = 1.47 eV) required the most energy input, with activation energy levels ranking as TS3 > TS1 > TS2.

However, step 4, $CH_2OH + OH \rightarrow CH_2 + H_2O + O$, in the methane synthesis process was endothermic (0.80 eV), and although it was endothermic, $CH_2 + OH \rightarrow CH_3 + O$ had a lower activation energy than all the other steps in both methanol and methane synthesis. This step also had a lower activation energy than the corresponding steps in methanol synthesis. We therefore concluded that the pathway to synthesize methane was thermodynamically more favorable, with CH_4 as the preferred product and methanol as the secondary result.

Table 5. The path resulting in CH_4 and CH_3OH. Energies are related to the CO in the gas phase plus the energy of three hydrogen atoms and one hydroxyl on the surface. The symbols in parentheses are the atoms added along the paths to balance the number of atoms during the reaction profile.

Path	Energy (eV)
CO(g) + (3H) + (OH)	0.00
CO + OH + (3H)	−1.35
TS1 + (3H)	1.13
HCO + O + (3H)	−1.30
HCO + OH + (2H)	−1.71
TS2 + (2H)	−1.23
CH_2O + O + (2H)	−1.30
CH_2O + OH + (H)	−2.39
TS3 + (H)	1.47
CH_2OH + O + (H)	−2.10
CH_2OH + OH (CH_4 pathway)	−2.77
CH_2OH + OH (CH_3OH pathway)	−2.91
TS4	−1.97
CH_2 + O + H_2O	−2.95
CH_2 + OH + (OH)	−1.94
TS5 + (OH)	−1.58
CH_3 + O + (OH)	−1.61
CH_3 + OH + (O)	−1.56
TS6 + (O)	−0.21
CH_4 + O + (O)	−0.85
CH_4(g) + (2O)	0.01
TS7	−1.25
CH_3OH + O	−1.71
CH_3OH(g) + (O)	−0.42

In the present investigation, a thorough examination was carried out on the synthesis of methane (CH_4) and methanol (CH_3OH) via the catalytic pathways illustrated by the overall reactions $CO + 6OH \rightarrow CH_4 + H_2O + 6O$ and $CO + 4OH \rightarrow CH_3OH + 4O$. These processes take place on the catalyst surface and are impacted by a number of variables, including the composition of the catalyst and the reaction conditions. In order to acquire insight into the fundamental mechanisms steering the generation of methane and methanol, we have systematically segmented the overall reactions into discrete stages, subsequently

analyzing the kinetics and thermodynamics of these steps. By investigating these individual steps, we have successfully elucidated the intricate pathways and mechanisms associated with the catalytic conversion processes of the conversion of CO to methane and methanol, including the identification of reaction intermediates, transition states, and rate-determining steps. In addition, a study of the kinetics and thermodynamics of each individual stage has allowed us to assess the catalytic efficacy under different conditions, where we found that the catalyst maintained its integrity unchanged throughout the catalytic cycles.

3. Computational Details

We have conducted periodic plane-wave DFT [40–42] calculations to examine the adsorption of CO and its reactivity on the surfaces of GO doped with manganese. All DFT calculations in our study were spin polarized calculations using the Vienna Ab initio Simulation Package (VASP) [72–74]. VASP provides approximate solutions to the many-body Schrödinger equation through DFT by solving the Kohn–Sham equations. Ion–electron interactions are represented by the projector-augmented wave (PAW) method [75,76]. To calculate the total energy, we have applied the Perdew–Burke–Ernzerhof (PBE) [77] variant of the generalized gradient approximation (GGA) [77]. The inclusion of the long-range Van der Waals (vdW) forces improves the energy description of each system [4,78–81] and we have therefore employed the DFT-D3 the method by Grimme as implemented in VASP [82]. The energies of the transition states (TS) are calculated using the nudged elastic band (NEB) [83] and dimer methods [84,85] implemented in VASP to climb up the potential energy surface from minimum to saddle points [86–88].

The adsorption energy of the adsorbates, E_{ads}, can be calculated as:

$$E_{ads} = E_{slab+mol} - E_{slab} - E_{mol} \qquad (1)$$

where $E_{slab+mol}$ is the energy of the relaxed surface with a relaxed adsorbed molecule, and E_{slab} and E_{mol} are the energies of the surface only and the molecule in vacuum, respectively.

The reaction energy of each reaction, $E_{reaction}$, can be calculated as:

$$E_{reaction} = E_{product} - E_{reactant} \qquad (2)$$

where $E_{product}$ and $E_{reactant}$ are the energies of the products and reactants, respectively.

The activation energy of each reaction, $E_{activation}$, can be calculated as:

$$E_{activation} = E_{transition-state} - E_{reactant} \qquad (3)$$

where the $E_{transition-state}$ and $E_{reactant}$ are the energies of the transition state and reactants of each reaction, respectively.

$$\Delta\rho = \rho_{AB} - \rho_A - \rho_B$$

where ρ_{AB} represent the charge densities of the combined graphene-OH system and ρ_A and ρ_B are the charge densities of the pristine graphene and the OH group of the combined structure, respectively.

During geometry optimization, we sampled the Brillouin zone using a $6 \times 6 \times 1$ special k-points grid, following the Monkhorst–Pack scheme [89,90]. The electron wave functions were expanded using plane waves with a cutoff energy of 450 eV for the graphene oxide structures. Geometry optimization ceased once the total energy converged within 10^{-5} eV, and the force exerted on each ion fell below 0.01 eV/Å. Figure 6 shows that the energy is converged at a k-points grid and cutoff energy of $6 \times 6 \times 1$ and 450 eV, respectively.
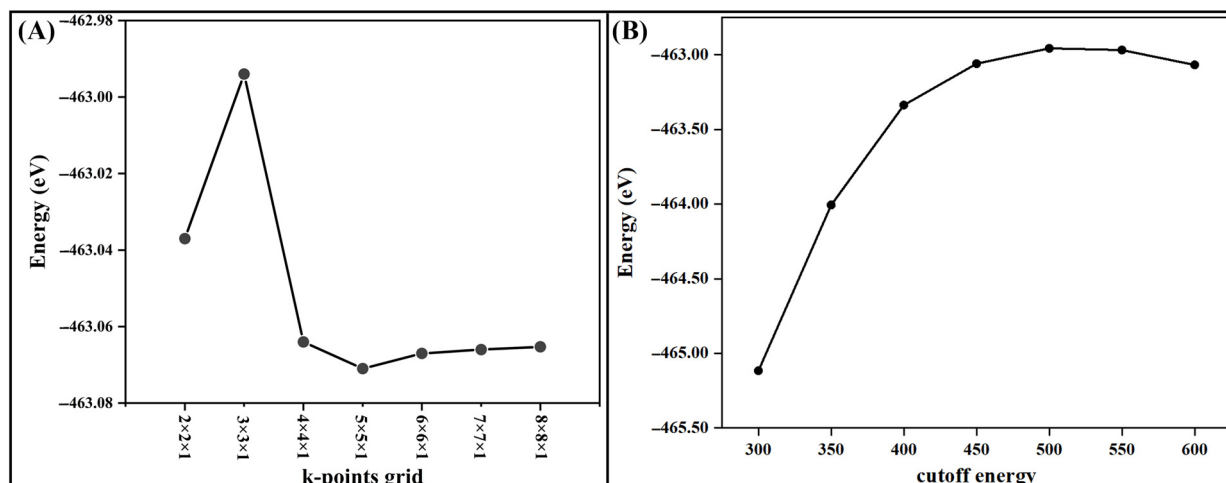
Figure 6. Graphs showing the energy convergence of graphene layer with respect to (**A**) k-points grid and (**B**) cutoff energy.

4. Conclusions

The hydrogenation method utilizes the GO surface as a source of hydrogen atoms, enabling the conversion of hydroxyl groups to epoxy groups within the mechanism. The use of manganese as an intermediate metal catalyst led to a negative absorption energy on graphene oxide. The molecules participating in the Fischer–Tropsch reactions release a significant amount of energy upon adsorption onto the surface, which facilitates the advancement of these reactions. By closely examining the reaction pathways for both products, it is possible to conclude that the significant energy released within the environment of the reaction corresponds to the activation energy required for each reaction and the heats of absorption along the pathways. The suitability of the catalyst is confirmed by these results, which explain the spontaneous progression of the reaction even along the steps with high activation energies. By comparing the calculated results with data from relevant sources, it is revealed that the use of GO as a surface material characterized by a larger surface area and lighter weight significantly increases the effectiveness of the required reactions. The activation energies of the chemical reactions affect the reaction rates, which means that faster reactions have lower activation energies.

The calculations further unveiled that the reaction that dictates the reaction rate featured the highest activation energy, underscoring the instability of this specific component within the process. Upon calculating the energies of each reaction's initial and final states, it was established that the reaction operated in an endothermic state. However, it is worth mentioning that in this study we have only investigated the reaction and activation energies, i.e., the thermodynamics and energy barriers, at 0 K using pure DFT.

Overall, the presence of manganese as a catalyst, along with the utilization of GO as a suitable surface possessing a substantial surface area and hosting hydroxyl and epoxy groups, proved efficient in expediting the reactions. Manganese, functioning as a valuable catalyst, facilitated the reactions more readily and effectively, converting carbon monoxide gas into the more advantageous and less harmful methane and methanol products, which have significant industrial applications. This mechanism offers potential for further exploration in practical applications, promising to mitigate environmental pollution and its associated consequences.

Author Contributions: Conceptualization, S.S.T.; methodology, S.S.T. and N.H.d.L.; software, S.S.T. and N.H.d.L.; validation, S.S.T. and N.H.d.L.; formal analysis, S.S.T.; investigation, H.B.; resources, S.S.T. and N.H.d.L.; data curation, H.B.; writing—original draft preparation, H.B.; writing—review and editing, M.T., S.S.T. and N.H.d.L.; visualization, H.B. and M.T.; supervision, S.S.T. and M.A.; project administration, S.S.T. and M.A.; funding acquisition, S.S.T. and N.H.d.L. All authors have read and agreed to the published version of the manuscript.

Data Availability Statement: The data that support the findings of this study are available from the corresponding author upon reasonable request.

Conflicts of Interest: The authors declare no conflicts of interest.

References

1. Perveen, S.; Kamruzzaman, M.; Yigitcanlar, T. What to assess to model the transport impacts of urban growth? A Delphi approach to examine the space–time suitability of transport indicators. *Int. J. Sustain. Transp.* **2018**, *13*, 597–613. [CrossRef]
2. Nourouzi, Z.; Chamani, A. Characterization of ambient carbon monoxide and PM 2.5 effects on fetus development, liver enzymes and TSH in Isfahan City, central Iran. *Environ. Pollut.* **2021**, *291*, 118238. [CrossRef]
3. World Health Organization. Why Urban Health Matters. 2010. Available online: https://www.who.int/publications/i/item/WHO-WKC-WHD-2010.1 (accessed on 13 September 2023).
4. Torkashvand, M.; Sarabadani Tafreshi, S.; de Leeuw, N.H. Density Functional Theory Study of the Hydrogenation of Carbon Monoxide over the Co(001) Surface: Implications for the Fischer–Tropsch Process. *Catalysts* **2023**, *13*, 837. [CrossRef]
5. Miroliaee, A.; Hoshdari, S.; Mohammadi Chahaki, M.M.; Abdouss, M. High surface area $ZnAl_2O_4$/reduced graphene oxide nanocomposites with enhanced photocatalytic performance. *Mater. Und Werkst.* **2019**, *50*, 140–154. [CrossRef]
6. Manisalidis, I.; Stavropoulou, E.; Stavropoulos, A.; Bezirtzoglou, E. Environmental and Health Impacts of Air Pollution: A Review. *Front. Public Health* **2020**, *8*, 505570. [CrossRef] [PubMed]
7. Pejhan, A.; Agah, J.; Adli, A.; Mehrabadi, S.; Raoufinia, R.; Mokamel, A.; Abroudi, M.; Ghalenovi, M.; Sadeghi, Z.; Bolghanabadi, Z.; et al. Exposure to air pollution during pregnancy and newborn liver function. *Chemosphere* **2019**, *226*, 447–453. [CrossRef]
8. Chen, R.; Pan, G.; Zhang, Y.; Xu, Q.; Zeng, G.; Xu, X.; Chen, B.; Kan, H. Ambient carbon monoxide and daily mortality in three Chinese cities: The China Air Pollution and Health Effects Study (CAPES). *Sci. Total. Environ.* **2011**, *409*, 4923–4928. [CrossRef]
9. Ibrahim, A.A. Carbon Dioxide and Carbon Monoxide Level Detector. In Proceedings of the 2018 21st International Conference of Computer and Information Technology (ICCIT), Dhaka, Bangladesh, 21–23 December 2018; pp. 1–5.
10. Voss, G.J.B.; Fløystad, J.B.; Voronov, A.; Rønning, M. The State of Nickel as Promotor in Cobalt Fischer–Tropsch Synthesis Catalysts. *Top. Catal.* **2015**, *58*, 896–904. [CrossRef]
11. Ashwell, A.P.; Lin, W.; Hofman, M.S.; Yang, Y.; Ratner, M.A.; Koel, B.E.; Schatz, G.C. Hydrogenation of CO to Methanol on Ni(110) through Subsurface Hydrogen. *J. Am. Chem. Soc.* **2017**, *139*, 17582–17589. [CrossRef]
12. Qi, Y.; Yang, J.; Chen, D.; Holmen, A. Recent Progresses in Understanding of Co-Based Fischer–Tropsch Catalysis by Means of Transient Kinetic Studies and Theoretical Analysis. *Catal. Lett.* **2014**, *145*, 145–161. [CrossRef]
13. Yang, J.; Qi, Y.; Zhu, J.; Zhu, Y.-A.; Chen, D.; Holmen, A. Reaction mechanism of CO activation and methane formation on Co Fischer–Tropsch catalyst: A combined DFT, transient, and steady-state kinetic modeling. *J. Catal.* **2013**, *308*, 37–49. [CrossRef]
14. Tan, K.F.; Xu, J.; Chang, J.; Borgna, A.; Saeys, M. Carbon deposition on Co catalysts during Fischer–Tropsch synthesis: A computational and experimental study. *J. Catal.* **2010**, *274*, 121–129. [CrossRef]
15. Cheng, J.; Hu, P.; Ellis, P.; French, S.; Kelly, G.; Lok, C.M. Density Functional Theory Study of Iron and Cobalt Carbides for Fischer−Tropsch Synthesis. *J. Phys. Chem. C* **2009**, *114*, 1085–1093. [CrossRef]
16. Williams, H.; Gnanamani, M.K.; Jacobs, G.; Shafer, W.D.; Coulliette, D. Fischer–Tropsch Synthesis: Computational Sensitivity Modeling for Series of Cobalt Catalysts. *Catalysts* **2019**, *9*, 857. [CrossRef]
17. Asiaee, A.; Benjamin, K.M. A density functional theory based elementary reaction mechanism for early steps of Fischer-Tropsch synthesis over cobalt catalyst. 1. Reaction kinetics. *Mol. Catal.* **2017**, *436*, 218–227. [CrossRef]
18. Javed, M.; Cheng, S.; Zhang, G.; Dai, P.; Cao, Y.; Lu, C.; Yang, R.; Xing, C.; Shan, S. Complete encapsulation of zeolite supported Co based core with silicalite-1 shell to achieve high gasoline selectivity in Fischer-Tropsch synthesis. *Fuel* **2017**, *215*, 226–231. [CrossRef]
19. Navas-Anguita, Z.; Cruz, P.L.; Martín-Gamboa, M.; Iribarren, D.; Dufour, J. Simulation and life cycle assessment of synthetic fuels produced via biogas dry reforming and Fischer-Tropsch synthesis. *Fuel* **2019**, *235*, 1492–1500. [CrossRef]
20. Ershov, M.; Potanin, D.; Gueseva, A.; Abdellatief, T.M.; Kapustin, V. Novel strategy to develop the technology of high-octane alternative fuel based on low-octane gasoline Fischer-Tropsch process. *Fuel* **2019**, *261*, 116330. [CrossRef]
21. Jamaati, M.; Torkashvand, M.; Tafreshi, S.S.; de Leeuw, N.H. A Review of Theoretical Studies on Carbon Monoxide Hydrogenation via Fischer–Tropsch Synthesis over Transition Metals. *Molecules* **2023**, *28*, 6525. [CrossRef]

22. Chen, C.; Wang, Q.; Wang, G.; Hou, B.; Jia, L.; Li, D. Mechanistic Insight into the C_2 Hydrocarbons Formation from Syngas on fcc-Co(111) Surface: A DFT Study. *J. Phys. Chem. C* **2016**, *120*, 9132–9147. [CrossRef]

23. Liu, J.-X.; Su, H.-Y.; Li, W.-X. Structure sensitivity of CO methanation on Co(0001), and surfaces: Density functional theory calculations. *Catal. Today* **2013**, *215*, 36–42. [CrossRef]

24. Petersen, M.A.; van den Berg, J.-A.; Ciobîcă, I.M.; van Helden, P. Revisiting CO Activation on Co Catalysts: Impact of Step and Kink Sites from DFT. *ACS Catal.* **2017**, *7*, 1984–1992. [CrossRef]

25. Zhang, M.; Chi, S.; Huang, H.; Yu, Y. Mechanism insight into MnO for CO activation and O removal processes on Co(0001) surface: A DFT and kMC study. *Appl. Surf. Sci.* **2021**, *567*, 150854. [CrossRef]

26. Montejo-Alvaro, F.; Alfaro-López, H.M.; Salinas-Juárez, M.G.; Rojas-Chávez, H.; Peralta-González, M.S.; Mondaca-Espinoza, F.J.; Cruz-Martínez, H. Metal clusters/modified graphene composites with enhanced CO adsorption: A density functional theory approach. *J. Nanoparticle Res.* **2022**, *25*, 11. [CrossRef]

27. Xu, L.; Yang, L.-M.; Ganz, E. Mn–graphene single-atom catalyst evaluated for CO oxidation by computational screening. *Theor. Chem. Accounts* **2018**, *137*, 98. [CrossRef]

28. Luo, M.; Liu, C.; Peera, S.G.; Liang, T. Atomic level N-coordinated Fe dual-metal embedded in graphene: An efficient double atoms catalyst for CO oxidation. *Colloids Surfaces A Physicochem. Eng. Asp.* **2021**, *621*, 126575. [CrossRef]

29. Liu, M.; Liu, C.; Luo, M.; Peera, S.G.; Liang, T. Theoretical study on iron and nitrogen co-doped graphene catalyzes CO oxidation. *Mol. Catal.* **2021**, *509*, 111624. [CrossRef]

30. Liu, M.; Liu, C.; Gouse Peera, S.; Liang, T. Catalytic oxidation mechanism of CO on FeN_2-doped graphene. *Chem. Phys.* **2022**, *559*, 111536. [CrossRef]

31. Fang, W.; Wang, C.; Liu, Z.; Wang, L.; Liu, L.; Li, H.; Xu, S.; Zheng, A.; Qin, X.; Liu, L.; et al. Physical mixing of a catalyst and a hydrophobic polymer promotes CO hydrogenation through dehydration. *Science* **2022**, *377*, 406–410. [CrossRef]

32. Li, Z.; Zhang, X.; Liu, J.; Shi, R.; Waterhouse, G.I.; Wen, X.; Zhang, T. Titania-Supported Ni_2P/Ni Catalysts for Selective Solar-Driven CO Hydrogenation. *Adv. Mater.* **2021**, *33*, 2103248. [CrossRef]

33. Ye, A.; Li, Z.; Ding, J.; Xiong, W.; Huang, W. Synergistic Catalysis of Al and Zn Sites of Spinel $ZnAl_2O_4$ Catalyst for CO Hydrogenation to Methanol and Dimethyl Ether. *ACS Catal.* **2021**, *11*, 10014–10019. [CrossRef]

34. Zhang, Z.; Chen, X.; Kang, J.; Yu, Z.; Tian, J.; Gong, Z.; Jia, A.; You, R.; Qian, K.; He, S.; et al. The active sites of Cu–ZnO catalysts for water gas shift and CO hydrogenation reactions. *Nat. Commun.* **2021**, *12*, 4331. [CrossRef] [PubMed]

35. Luo, M.; Liang, Z.; Liu, C.; Qi, X.; Chen, M.; Ur Rehman Sagar, R.; Yang, H.; Liang, T. Single–atom manganese and nitrogen co-doped graphene as low-cost catalysts for the efficient CO oxidation at room temperature. *Appl. Surf. Sci.* **2020**, *536*, 147809. [CrossRef]

36. Luo, M.; Liang, Z.; Gouse Peera, S.; Chen, M.; Liu, C.; Yang, H.; Liu, J.; Pramod Kumar, U.; Liang, T. Theoretical study on the adsorption and predictive catalysis of MnN4 embedded in carbon substrate for gas molecules. *Appl. Surf. Sci.* **2020**, *525*, 146480. [CrossRef]

37. Ray, S.C. Application and Uses of Graphene Oxide and Reduced Graphene Oxide. In *Applications of Graphene and Graphene-Oxide Based Nanomaterials*; Elsevier: Amsterdam, The Netherlands, 2015; pp. 39–55.

38. Majumdar, B.; Sarma, D.; Bhattacharya, T.; Sarma, T.K. Graphene Oxide as Metal-Free Catalyst in Oxidative Dehydrogenative C–N Coupling Leading to α-Ketoamides: Importance of Dual Catalytic Activity. *ACS Sustain. Chem. Eng.* **2017**, *5*, 9286–9294. [CrossRef]

39. Dideikin, A.T.; Vul', A.Y. Graphene Oxide and Derivatives: The Place in Graphene Family. *Front. Phys.* **2019**, *6*, 149. [CrossRef]

40. Ahmad, H.; Fan, M.; Hui, D. Graphene oxide incorporated functional materials: A review. *Compos. Part B Eng.* **2018**, *145*, 270–280. [CrossRef]

41. Dreyer, D.R.; Park, S.; Bielawski, C.W.; Ruoff, R.S. The chemistry of graphene oxide. *Chem. Soc. Rev.* **2009**, *39*, 228–240. [CrossRef] [PubMed]

42. Gao, W. *Graphene Oxide*; Springer International Publishing: Cham, Switzerland, 2015.

43. Lahaye, R.J.W.E.; Jeong, H.K.; Park, C.Y.; Lee, Y.H. Density functional theory study of graphite oxide for different oxidation levels. *Phys. Rev. B* **2009**, *79*, 125435. [CrossRef]

44. Mihet, M.; Dan, M.; Lazar, M.D. CO_2 Hydrogenation Catalyzed by Graphene-Based Materials. *Molecules* **2022**, *27*, 3367. [CrossRef]

45. Derekaya, F.; Köprülü, A.B.; Kilinç, Y.S. Investigation of CO Methanation with Different Carbon-Supported Ni-, Fe-, and Co-Containing Catalysts. *Arab. J. Sci. Eng.* **2023**, *48*, 8989–9008. [CrossRef]

46. Tsiotsias, A.I.; Charisiou, N.D.; Yentekakis, I.V.; Goula, M.A. Bimetallic Ni-Based Catalysts for CO_2 Methanation: A Review. *Nanomaterials* **2020**, *11*, 28. [CrossRef]

47. Mebrahtu, C.; Krebs, F.; Perathoner, S.; Abate, S.; Centi, G.; Palkovits, R. Hydrotalcite based Ni–Fe/(Mg, Al)O_x catalysts for CO_2 methanation—Tailoring Fe content for improved CO dissociation, basicity, and particle size. *Catal. Sci. Technol.* **2018**, *8*, 1016–1027. [CrossRef]

48. Gui, Y.; Peng, X.; Liu, K.; Ding, Z. Adsorption of C_2H_2, CH_4 and CO on Mn-doped graphene: Atomic, electronic, and gas-sensing properties. *Phys. E Low-Dimens. Syst. Nanostructures* **2020**, *119*, 113959. [CrossRef]

49. Wei, Y.; Luo, D.; Yan, L.; Ma, C.; Fu, Z.; Guo, L.; Cai, M.; Sun, S.; Zhang, C. Boosting CO Hydrogenation Performance of Facile Organics Modified Iron Oxide/Reduced Graphene Oxide Catalysts. *Catal. Lett.* **2021**, *152*, 1835–1843. [CrossRef]

50. Guo, L.; Gao, X.; Gao, W.; Wu, H.; Wang, X.; Sun, S.; Wei, Y.; Kugue, Y.; Guo, X.; Sun, J.; et al. High-yield production of liquid fuels in CO_2 hydrogenation on a zeolite-free Fe-based catalyst. *Chem. Sci.* **2022**, *14*, 171–178. [CrossRef]

51. Liu, W.; Cheng, S.; Malhi, H.S.; Gao, X.; Zhang, Z.; Tu, W. Hydrogenation of CO_2 to Olefins over Iron-Based Catalysts: A Review. *Catalysts* **2022**, *12*, 1432. [CrossRef]

52. Liang, B.; Sun, T.; Ma, J.; Duan, H.; Li, L.; Yang, X.; Zhang, Y.; Su, X.; Huang, Y.; Zhang, T. Mn decorated Na/Fe catalysts for CO_2 hydrogenation to light olefins. *Catal. Sci. Technol.* **2018**, *9*, 456–464. [CrossRef]

53. Huang, J.; Zhang, G.; Wang, M.; Zhu, J.; Ding, F.; Song, C.; Guo, X. The synthesis of higher alcohols from CO_2 hydrogenation over Mn-Cu-K modified Fe_5C_2 and CuZnAlZr tandem catalysts. *Front. Energy Res.* **2023**, *10*, 995800. [CrossRef]

54. Zafari, R.; Abdouss, M.; Zamani, Y. Effect of Mn and reduced graphene oxide for the Fischer–Tropsch reaction: An efficient catalyst for the production of light olefins from syngas. *React. Kinet. Catal. Lett.* **2020**, *129*, 707–724. [CrossRef]

55. Boukhvalov, D. Carbon Mono and Dioxide Hydrogenation over Pure and Metal Oxide Decorated Graphene Oxide Substrates: Insight from DFT. *Graphene* **2013**, *2*, 109–114. [CrossRef]

56. Kim, S.; Zhou, S.; Hu, Y.; Acik, M.; Chabal, Y.J.; Berger, C.; De Heer, W.; Bongiorno, A.; Riedo, E. Room-temperature metastability of multilayer graphene oxide films. *Nat. Mater.* **2012**, *11*, 544–549. [CrossRef] [PubMed]

57. Zhu, J.; Andres, C.M.; Xu, J.; Ramamoorthy, A.; Tsotsis, T.; Kotov, N.A. Pseudonegative Thermal Expansion and the State of Water in Graphene Oxide Layered Assemblies. *ACS Nano* **2012**, *6*, 8357–8365. [CrossRef] [PubMed]

58. Sun, X.; Luan, S.; Shen, H.; Lei, S. Effect of metal doping on carbon monoxide adsorption on phosphorene: A first-principles study. *Superlattices Microstruct.* **2018**, *124*, 168–175. [CrossRef]

59. Ren, B.; Dong, X.; Yu, Y.; Wen, G.; Zhang, M. A density functional theory study on the carbon chain growth of ethanol formation on Cu-Co(111) and (211) surfaces. *Appl. Surf. Sci.* **2017**, *412*, 374–384. [CrossRef]

60. Qi, K.-Z.; Wang, G.-C.; Zheng, W.-J. A first-principles study of CO hydrogenation into methane on molybdenum carbides catalysts. *Surf. Sci.* **2013**, *614*, 53–63. [CrossRef]

61. Ammar, H.Y. CH_2O adsorption on M (M = Li, Mg and Al) atom deposited ZnO nano-cage: DFT study. *Key Eng. Mater.* **2018**, *786*, 384–392. [CrossRef]

62. Zhang, Y.; Xu, X. Predictions of adsorption energies of methane-related species on Cu-based alloys through machine learning. *Mach. Learn. Appl.* **2020**, *3*, 100010. [CrossRef]

63. Taylor, C.J.; Pomberger, A.; Felton, K.C.; Grainger, R.; Barecka, M.; Chamberlain, T.W.; Bourne, R.A.; Johnson, C.N.; Lapkin, A.A. A Brief Introduction to Chemical Reaction Optimization. *Chem. Rev.* **2023**, *123*, 3089–3126. [CrossRef] [PubMed]

64. Pham, T.H.M.; Ko, Y.; Wei, M.; Zhao, K.; Zhong, L.; Züttel, A. Understanding the role of surface oxygen-containing functional groups on carbon-supported cobalt catalysts for the oxygen evolution reaction. *J. Mater. Chem. A* **2023**, *11*, 21066–21077. [CrossRef]

65. Etim, U.J.; Zhang, C.; Zhong, Z. Impacts of the Catalyst Structures on CO_2 Activation on Catalyst Surfaces. *Nanomaterials* **2021**, *11*, 3265. [CrossRef]

66. Qiu, K.; Chai, G.; Jiang, C.; Ling, M.; Tang, J.; Guo, Z.X. Highly Efficient Oxygen Reduction Catalysts by Rational Synthesis of Nanoconfined Maghemite in a Nitrogen-Doped Graphene Framework. *ACS Catal.* **2016**, *6*, 3558–3568. [CrossRef]

67. Khanra, B.; Bertolini, J.; Rousset, J. Effect of surface segregation on the catalytic activity of alloys: CO hydrogenation on Pd–Ni(111) surface. *J. Mol. Catal. A Chem.* **1998**, *129*, 233–240. [CrossRef]

68. Nakamura, H.; Curran, H.J.; Polo Córdoba, A.; Pitz, W.J.; Dagaut, P.; Togbé, C.; Sarathy, S.M.; Mehl, M.; Agudelo Santamaría, J.R.; Bustamante, F. An experimental and modeling study of diethyl carbonate oxidation. *Combust. Flame* **2015**, *162*, 1395–1405. [CrossRef]

69. Maryunina, K.; Letyagin, G.; Bogomyakov, A.; Morozov, V.; Tumanov, S.; Veber, S.; Fedin, M.; Saverina, E.; Syroeshkin, M.; Egorov, M.; et al. Re(i)-nitroxide complexes. *RSC Adv.* **2021**, *11*, 19902–19907. [CrossRef] [PubMed]

70. Reuter, C.B.; Zhang, R.; Yehia, O.R.; Rezgui, Y.; Ju, Y. Counterflow flame experiments and chemical kinetic modeling of dimethyl ether/methane mixtures. *Combust. Flame* **2018**, *196*, 1–10. [CrossRef]

71. Chang, C.-R.; Long, B.; Yang, X.-F.; Li, J. Theoretical Studies on the synergetic effects of Au–Pd bimetallic catalysts in the selective oxidation of methanol. *J. Phys. Chem. C* **2015**, *119*, 16072–16081. [CrossRef]

72. Kresse, G.; Furthmüller, J. Efficiency of ab-initio total energy calculations for metals and semiconductors using a plane-wave basis set. *Comput. Mater. Sci.* **1996**, *6*, 15–50. [CrossRef]

73. Kresse, G.; Hafner, J. Norm-conserving and ultrasoft pseudopotentials for first-row and transition elements. *J. Phys. Condens. Matter* **1994**, *6*, 8245–8257. [CrossRef]

74. Kresse, G.; Hafner, J. Ab initio molecular dynamics for liquid metals. *Phys. Rev. B* **1993**, *47*, 558–561. [CrossRef]

75. Blöchl, P.E. Projector augmented-wave method. *Phys. Rev. B* **1994**, *50*, 17953–17979. [CrossRef] [PubMed]

76. Kresse, G.; Joubert, D. From ultrasoft pseudopotentials to the projector augmented-wave method. *Phys. Rev. B* **1999**, *59*, 1758–1775. [CrossRef]

77. Perdew, J.P.; Burke, K.; Ernzerhof, M. Generalized Gradient Approximation Made Simple. *Phys. Rev. Lett.* **1996**, *77*, 3865–3868. [CrossRef] [PubMed]

78. Sarabadani Tafreshi, S.; Ranjbar, M.; Taghizade, N.; Panahi, S.F.K.S.; Jamaati, M.; de Leeuw, N.H. A First-Principles Study of CO_2 Hydrogenation on a Niobium-Terminated NbC(111) Surface. *Chemphyschem* **2022**, *23*, e202100781. [CrossRef]

79. Sarabadani Tafreshi, S.; Panahi, S.; Fatemeh, K.S.; Taghizade, N.; Jamaati, M.; Ranjbar, M.; de Leeuw, N.H. Thermodynamic and Kinetic Study of Carbon Dioxide Hydrogenation on the Metal-Terminated Tantalum-Carbide (111) Surface: A DFT Calculation. *Catalysts* **2022**, *12*, 1275. [CrossRef]

80. Sarabadani Tafreshi, S.; Ranjbar, M.; Jamaati, M.; Panahi, S.F.K.S.; Taghizade, N.; Torkashvand, M.; de Leeuw, N.H. Carbon dioxide hydrogenation over the carbon-terminated niobium carbide (111) surface: A density functional theory study. *Phys. Chem. Chem. Phys.* **2022**, *25*, 2498–2509. [CrossRef] [PubMed]

81. Sarabadani Tafreshi, S.; Taghizade, N.; Sharifian, M.; Panahi, S.F.K.S.; Torkashvand, M.; de Leeuw, N.H. A density functional theory study of CO_2 hydrogenation on carbon-terminated TaC(111) surface. *React. Kinet. Catal. Lett.* **2023**, *136*, 1945–1963. [CrossRef]

82. Grimme, S.; Ehrlich, S.; Goerigk, L. Effect of the Damping Function in Dispersion Corrected Density Functional Theory. *J. Comput. Chem.* **2011**, *32*, 1456. [CrossRef]

83. Henkelman, G.; Uberuaga, B.P.; Jónsson, H. A climbing image nudged elastic band method for finding saddle points and minimum energy paths. *J. Chem. Phys.* **2000**, *113*, 9901–9904. [CrossRef]

84. Henkelman, G.; Jónsson, H. A dimer method for finding saddle points on high dimensional potential surfaces using only first derivatives. *J. Chem. Phys.* **1999**, *111*, 7010–7022. [CrossRef]

85. Heyden, A.; Bell, A.T.; Keil, F.J. Efficient methods for finding transition states in chemical reactions: Comparison of improved dimer method and partitioned rational function optimization method. *J. Chem. Phys.* **2005**, *123*, 224101. [CrossRef] [PubMed]

86. Olsen, R.A.; Kroes, G.J.; Henkelman, G.; Arnaldsson, A.; Jónsson, H. Comparison of methods for finding saddle points without knowledge of the final states. *J. Chem. Phys.* **2004**, *121*, 9776–9792. [CrossRef] [PubMed]

87. Xiao, P.; Sheppard, D.; Rogal, J.; Henkelman, G. Solid-state dimer method for calculating solid-solid phase transitions. *J. Chem. Phys.* **2014**, *140*, 174104. [CrossRef] [PubMed]

88. Kästner, J.; Sherwood, P. Superlinearly converging dimer method for transition state search. *J. Chem. Phys.* **2008**, *128*, 014106. [CrossRef] [PubMed]

89. Wisesa, P.; McGill, K.A.; Mueller, T. Efficient generation of generalized Monkhorst-Pack grids through the use of informatics. *Phys. Rev. B* **2016**, *93*, 155109. [CrossRef]

90. Monkhorst, H.J.; Pack, J.D. Special points for Brillouin-zone integrations. *Phys. Rev. B* **1976**, *13*, 5188–5192. [CrossRef]